



# Superplastic deformation and energy dissipation mechanism in surface-bonded carbon nanofibers



Jingjun Gu<sup>a</sup>, Frederic Sansoz<sup>a,b,\*</sup>

<sup>a</sup> School of Engineering, The University of Vermont, Burlington, VT 05405, United States

<sup>b</sup> Materials Science Program, The University of Vermont, Burlington, VT 05405, United States

## ARTICLE INFO

### Article history:

Received 19 September 2014

Received in revised form 12 December 2014

Accepted 20 December 2014

### Keywords:

Carbon nanofibers

Superplasticity

Fracture

Deformation mechanisms

Atomistic simulation

## ABSTRACT

Molecular dynamics simulations are used to understand the role of surface C–C bonds formed by heat treatment on plastic deformation and fracture mechanisms in cone-stacked carbon nanofibers. The simulations predict that the surface bond density linearly relates to the heat treatment temperature. As the surface bond density increases, it is found that tensile strength and ductile fracture energy in carbon nanofibers rise dramatically by more than 65% and 622%, respectively; hence unveiling a regime of superplastic deformation that is unmatched by standard carbon nanotubes and graphitic nanofibers. We demonstrate that both strengthening and superplasticity effects are enabled by the occurrence of surface bond-induced fiber splaying processes that can effectively resist interlayer sliding and crack propagation during deformation. The findings of this computational study have important implications for designing flaw-tolerant nanocomposite systems.

© 2015 Elsevier B.V. All rights reserved.

## 1. Introduction

Vapor-grown carbon nanofibers (VG-CNFs) represent a technologically important class of low-dimensional nanomaterials primarily used as nanocomposite reinforcing fillers [1], catalyst supports [2] and electrode materials for energy storage devices [3]. Small amounts of VG-CNFs in polymer matrix composite materials enhance failure strength and fracture toughness dramatically without compromising the ductility [4,5]. At the microscopic scale, CNFs are comprised of oblique graphene layers with a concentric cone-stacked morphology [6,7] that confers greater sliding resistance and strength to the fiber-matrix interface than carbon nanotubes (CNTs) [8,9]. Recent experimental evidence [5] shows that crack-bridging CNFs can significantly augment the fracture energy required to propagate a crack in a polymer matrix because of the conical structure unravelling continuously without breaking during crack tip opening. However, meaningful results on the mechanical performance of CNF-based nanocomposites can be achieved only if the influence of surface bonds on the mechanical behavior of CNFs is fully understood [10–13]. In particular, previous studies [14–17] have shown evidence for large statistical dispersions in failure strength between fibers subjected to the same heat

treatment. It has been found that fractured CNFs could exhibit either brittle-like protruding cone profiles from layer sliding [15] or energy-dissipating ductile mechanisms [5] depending on the surface characteristics; yet the role of surface bonds on these important fracture processes has never been clearly established. The present molecular dynamics (MD) study gives new insight into the fundamental relationship between surface bonds and fracture mechanisms in cone-stacked CNFs, and reports a unique regime of superplasticity from surface bond reconstruction at the nanoscale that can be easily controlled by the heat treatment temperature.

## 2. Computational methods

### 2.1. Molecular dynamics simulations

Fig. 1a displays a representative atomic model for the simulation of surface-bonded CNFs. The MD simulation software LAMMPS [18] was used with an adaptive intermolecular reactive empirical bond order potential [19]. Each CNF was made of 112.9° stacked-cones, and was 7.5 nm in diameter and 22.8 nm in length, as shown in Fig. 1b. One  $sp^3$  bond was added randomly between each  $sp^2$ -bonded graphene cone to account for the effects of layer cross-linking from  $sp^3$ -bond bridging [20,21], as shown in Label A in Fig. 1b. Periodic boundary conditions were used in the fiber direction with other directions kept free. The formation of surface C–C

\* Corresponding author at: School of Engineering, The University of Vermont, Burlington, VT 05405, United States. Tel.: +1 802 656 3837.

E-mail address: [frederic.sansoz@uvm.edu](mailto:frederic.sansoz@uvm.edu) (F. Sansoz).

bonds such as  $sp$  and  $sp^2$  bonds, Label B in Fig. 1b, was performed thermodynamically by non-equilibrium MD simulations of a pristine CNF following our previous methodology [16]. The surface structure on the CNF initially consisted of active open edges. At high temperature, active sites are able to overcome the energy barrier to form closed loops between adjacent graphene cones from either single-dangling bonds or the folding of graphene bilayer edges [12,13,16,22–24]. Different thermal cycles were simulated by varying the maximum hold temperature from 400 K to 2273 K under zero pressure in the isothermal–isobaric ensemble (constant number of particles, pressure and temperature, NPT). After heating and return to 300 K, tensile deformation was simulated by straining the simulation box along the fiber axis at a constant strain rate of  $1.0 \times 10^8 \text{ s}^{-1}$  in the NVT ensemble (constant number of particles, volume and temperature) with a Nosé–Hoover thermostat maintained at 300 K and a time step of 2 fs. Details on the simulation methods and stress calculations, as well as the identification of surface bonds formed, can be found elsewhere [16]. Analysis of bond deformation at different applied strains was conducted with the atomistic visualization software Ovito [25]. In the following, the number of surface C–C bonds measured per unit length along the axis will be referred to as the surface bond density  $N$ .

For comparison purposes, we have also simulated the mechanical response of a graphitic CNF because, experimentally, they represent a widespread example of extreme surface bonding and graphitization for heat-treated VG-CNFs. These fibers are typically

made of inner conical layers surrounded by sidewalls resembling a straight multi-walled CNT [13,22]. Here, the graphitic structure was simulated by tightly inserting a pristine CNF into a double-walled CNT of equivalent size, heat treated at 2273 K under zero stress.

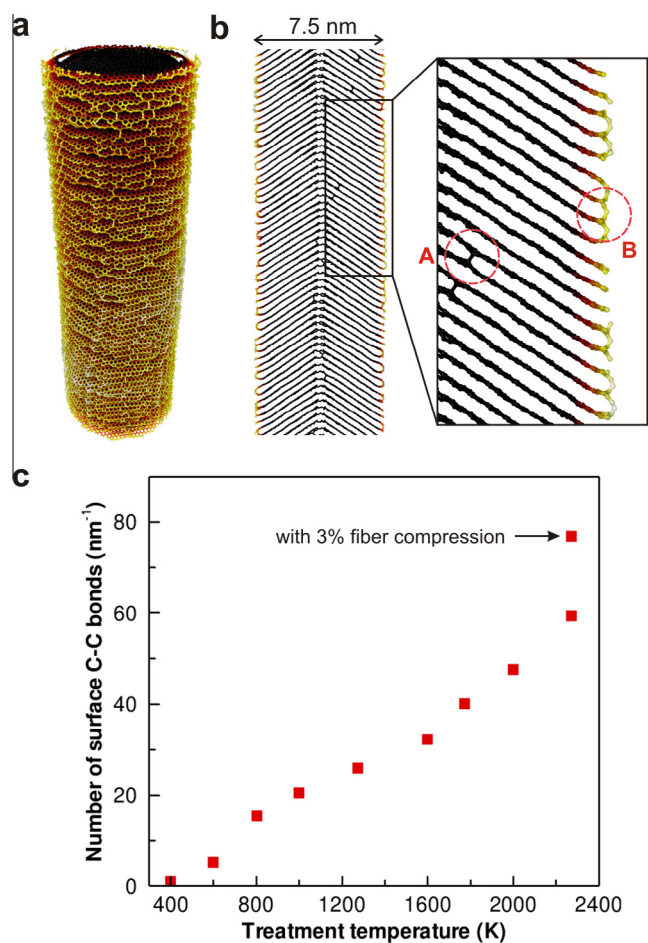
## 2.2. Finite-element analysis of fracture energy

To study the effects of surface bond distribution on strain energy release rate during crack propagation in CNFs, simplified linear-elastic continuum models for cone-stacked CNFs containing potential surface cracks of different size and distribution were created using the finite element analysis (FEA) software ABAQUS. A three-dimensional cylindrical FEA model of 3.8 nm in diameter ( $D$ ) and 22.8 nm in height was used. The fiber was meshed using 2800 brick and wedge elements corresponding to 10 element slices or stacked graphene layers. Each graphene layer was represented by a flat circular disk with a thickness equal to one brick element. The fiber density was  $2000 \text{ kg/m}^3$ . Young's modulus was 20 GPa and Poisson's ratio was 0.23, based on the atomistic simulation results of the present study. The bottom surface of the fiber was fixed in all directions, while the top surface was displaced by applying a concentrated force of 90.7 nN that was the average force predicted in the atomistic CNF models at the yielding point. For simplicity, we assumed a constant crack density of 25% between every 2 layers. The crack density was defined as the ratio of total surface crack length over the fiber perimeter ( $\pi D$ ) and was equal to  $1 - N$ . Two surface crack lengths, either  $\pi D/20$  or  $\pi D/40$ , were considered by partitioning each circular disk into 20 or 40 wedges, respectively. The local tensile stress was calculated by linear geometric order and reduced integration. The strain energy release rate was computed on a single crack using the contour path  $J$ -integral [26].

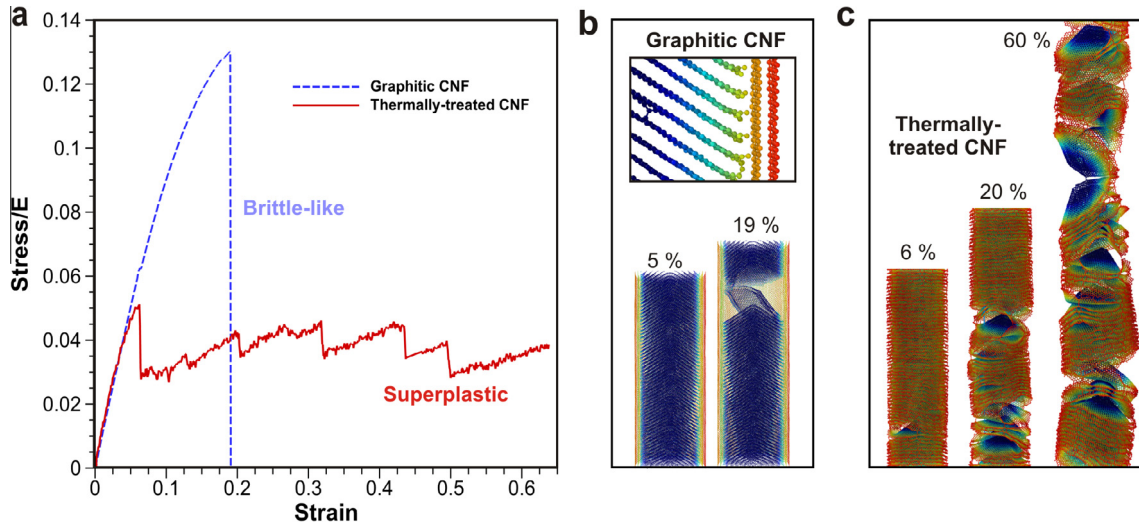
## 3. Results and discussion

Fig. 1c shows that the surface bond density grows almost linearly with the heat-treatment temperature, attaining  $\sim 59 \text{ bonds nm}^{-1}$  at 2273 K. This figure also suggests that a 3% fiber pre-compression at 2273 K can further increase the surface bond density by 30% due to the reduction in interval distance between the graphene cones.

The representative mechanical response of a thermally-treated, surface-bonded CNF simulated by MD is presented in Fig. 2 and compared to that of a graphitic CNF structure. Here thermal treatment was performed at 1273 K resulting in  $\sim 26 \text{ surface bonds nm}^{-1}$ . Fig. 2a reveals marked differences in the fracture behavior of these two types of fiber. On one hand, a graphitic CNF is found to deform elastically and fail in a brittle-like manner at a strain limit of 19%, consistent with deformation and failure mechanisms observed on multi-walled CNTs in past *in-situ* TEM experiments [21]. Fig. 2b shows that fracture in graphitic CNFs starts by the propagation of a single crack nucleated in the inner core with instantaneous load transfer to the double-walled CNT layer. The brittle failure of graphitic CNFs can therefore be attributed to the cleavage of  $sp^2$  bonds in the outer layer, which also agrees well with a previous experimental study from nanoindentation testing of VG-CNFs [14]. On the other hand, the simulated response of the heat-treated CNF with  $26 \text{ surface bonds nm}^{-1}$ , Fig. 2a, gives rise to a lower elastic limit at 6% and significant superplasticity characterized by prolonged plastic deformation exceeding 64% and serrated plastic flow. We note that the simulation was interrupted after reaching its own time limit, so it is possible for the fiber to have reached further plastic strain. Nevertheless, such mechanical characteristics are unmatched by



**Fig. 1.** Atomistic modeling of surface-bonded cone-stacked CNFs. (a) Equilibrium microstructure of a CNF heat-treated at 2273 K. (b) Skeleton of the structure showing both internal and surface bonds, Labels A and B, respectively. (c) Surface bond density as a function of heat treatment temperature. Arrow indicates that a 3% compression strain was applied during thermal treatment at 2273 K.



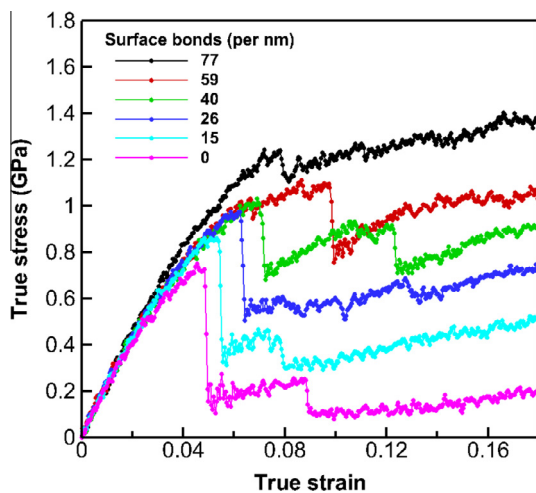
**Fig. 2.** Comparison of mechanical behavior between a graphitic CNF similar to those in experiments and a thermally-treated CNF with a surface bond density of 26 bonds per nm predicted by MD simulations. (a) Tensile stress and strain curves at 300 K normalized by Young's modulus. (b) Close-up view of internal and surface bond structure and atomistic snapshots of failure processes in a graphitic CNF. (c) Atomistic snapshots of failure processes in a thermally-treated, surface-bonded CNF.

standard CNTs and graphitic nanofibers. Fig. 2c shows that the underlying plastic deformation process is more homogeneously distributed than in graphitic fibers. The fracture process begins with the nucleation of small surface cracks from layer debonding, and continues with the unraveling of conical layers, but no catastrophic failure.

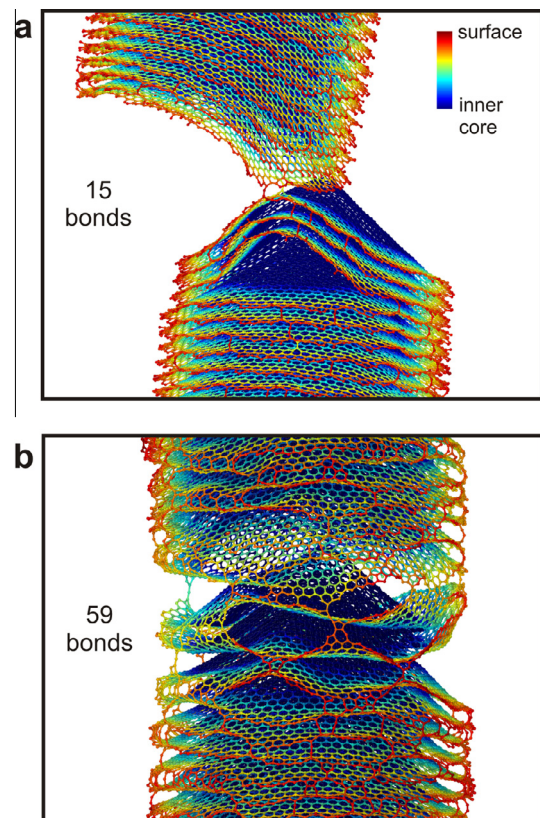
Furthermore, in Fig. 3, we find a strong influence of the surface bond density on superplastic deformation and fracture behavior in surface-bonded CNFs when simulating different densities from 0 to 77 bonds  $\text{nm}^{-1}$ . Apparently, the stress–strain curves in this figure shows that a CNF with no thermal treatment or zero surface bonds displays obvious brittleness with a stress drop near zero after yielding, because the load is suddenly transferred to the very few cross-linking  $sp^3$ -bonds added between the layers. By way of contrast, Fig. 3 demonstrates a steady increase in both tensile strength and ductility as the surface bond density increases.

Fig. 4a reveals that the atomic deformation mechanism in a CNF with low surface bond density (15 bonds  $\text{nm}^{-1}$ ) is associated with the propagation of a large localized crack produced by the sliding of two adjacent graphene cones. This process leaves no apparent

plastic deformation and is predominantly governed by the dissipation of weak van-der-Waals interactions between layers [5,27,28]. On the contrary, the atomistic snapshot obtained on a CNF populated by more abundant surface bonds (59 bonds  $\text{nm}^{-1}$ ) shows in Fig. 4b that plasticity is more distributed and involves the splaying of the fiber by initiation of multiple surface microcracks. We have determined that the average size of the surface flaws formed at the



**Fig. 3.** Effect of surface bond density on tensile stress–strain curves of CNFs under uniaxial deformation at a constant strain rate ( $1.0 \times 10^8 \text{ s}^{-1}$ ). An increasing surface bond density was produced by using different thermal and pre-compression treatments.



**Fig. 4.** Effects of surface bond density on atomic-scale fracture mechanisms of surface-bonded CNFs at an applied strain of 14%. (a) Interlayer sliding and localized crack propagation in a CNF with 15 surface bonds per nm. (b) Surface bond-induced splaying process in a CNF with 59 surface bonds per nm.

yield point decreases as the surface bond density increases. It is also worth mentioning that, in Fig. 3, the stress–strain curves for fibers associated with strong surface bond-induced splaying effects are similar to those predicted in the deformation and fracture of “super” CNT structures characterized by “fishing net” effects [29].

To further understand the atomistic results, we quantitatively examined in Fig. 5 how fracture strength and energy dissipation vary with the surface bond density. Fig. 5a shows that the limit of elasticity is improved by more than 65% from 0.75 GPa to 1.24 GPa owing to the formation of surface bonds during thermal and pre-compression treatments. Notably, this figure suggests a linear trend between limit of elasticity and surface bond density. To explain this behavior, we propose to model the CNF as a core–shell composite system where the core is defined by the cone-stacked backbone structure, excluding all surface atoms, which are then considered as parts of the shell. Due to non-uniform surface bonding, the shell can be viewed as an atomically-thin, porous layer. Thus it is possible to predict the overall fiber strength  $\sigma_y$  such as:

$$\sigma_y = V_f \sigma_b + (1 - V_f) \sigma_c, \quad (1)$$

where  $\sigma_b$  and  $\sigma_c$  are the strength of a single surface bond and the core strength, respectively, and  $V_f$  is the volume fraction of surface bonds.  $V_f$  is also related to the surface bond density  $N$  by:

$$V_f = N(A_b/A_f) \quad (2)$$

with  $A_b$  and  $A_f$  the cross-sectional areas for a C–C single bond ( $1.5 \times 10^{-2} \text{ nm}^2$ ) and our fiber ( $44.2 \text{ nm}^2$ ), respectively. Substituting (2) in (1) leads to:

$$\sigma_y = N \frac{A_b}{A_f} (\sigma_b - \sigma_c) + \sigma_c \quad (3)$$

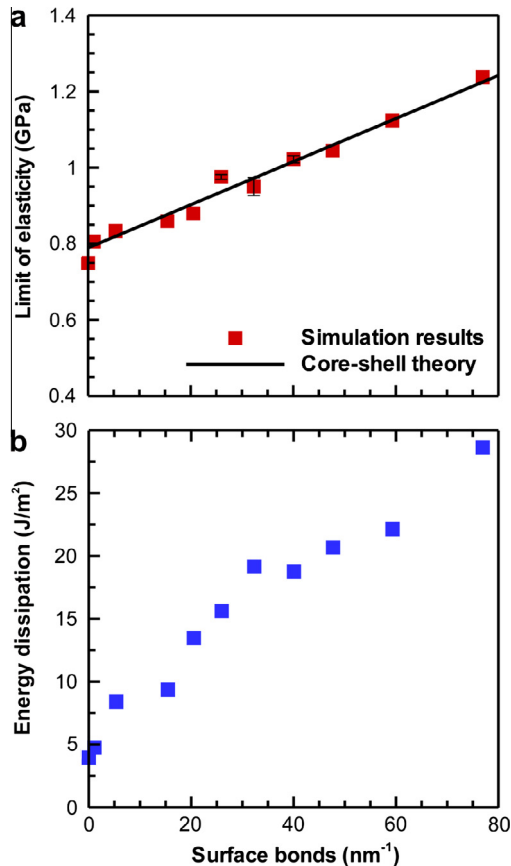


Fig. 5. Effects of surface bond density  $N$  on (a) limit of elasticity and (b) energy dissipation from plastic deformation in surface-bonded CNFs.

Assuming that  $A_f$ ,  $A_b$ ,  $\sigma_b$  and  $\sigma_c$  are constant, the fiber strength is found to be proportional to  $N$ . We calculated from Eq. (3) that the core strength associated with the weak van-der-Waals interactions competing against the interlayer decohesion is  $\sigma_c = 0.78 \text{ GPa}$ , using the intercept of the fitting line with the  $y$ -axis in Fig. 5a. Also taking into account the slope of the fitting line in Fig. 5a enabled us to find that the tensile strength for a single surface bond is  $\sigma_b = 15 \text{ GPa}$ . Therefore these estimates prove that surface bonds not only play a major strengthening role in CNFs, but also are extremely difficult to break apart in the process of surface splaying associated with superplastic deformation.

Furthermore, Fig. 5b presents the energy dissipated in plastic deformation during failure, which was calculated from Fig. 3 by integrating the stress–strain curves after the elastic limit and dividing by the applied plastic strain. Fig. 5b shows that the fracture energy released dramatically increases from  $3.96 \text{ J/m}^2$  to  $28.63 \text{ J/m}^2$  corresponding to a 622% enhancement, and attains values that are significantly higher than the critical energy release reported for standard PAN-based carbon fibers,  $\sim 7 \text{ J/m}^2$  [30]. These results strongly suggest that surface bond reconstruction is conducive to making CNFs stronger and more resistant to crack propagation at the same time.

A simplified continuum analysis presented in Fig. 6 was used to interpret this effect. Here, we imagine that the skin of a CNF has a surface bond density  $N$  resulting to a  $1 - N$  surface crack density. We also assume that the surface flaws only propagate between graphene layers perpendicularly to the loading direction and that for a given  $N$ , the total crack area is constant regardless of the average size and distribution of the flaws. Fig. 6a and b proves that different surface flaw distributions do not significantly change the predicted contour path integral  $J_0$  or strain energy release rate. Furthermore, it has been shown theoretically that bonding from bilayer edge folding occur at specific sites that are well-spread over the surface of CNFs [16]. Therefore cases where surface cracks would be localized on one side of the fiber are statistically limited. However, average surface crack length and total crack area have been found to decrease when  $N$  increases, which is expected to lead to a concomitant decrease in strain energy release rate. This hypothesis is supported by the results in Fig. 6c showing that there is a pronounced increase in energy release rate for larger surface cracks. Concurrently, the critical energy release rate, or fracture

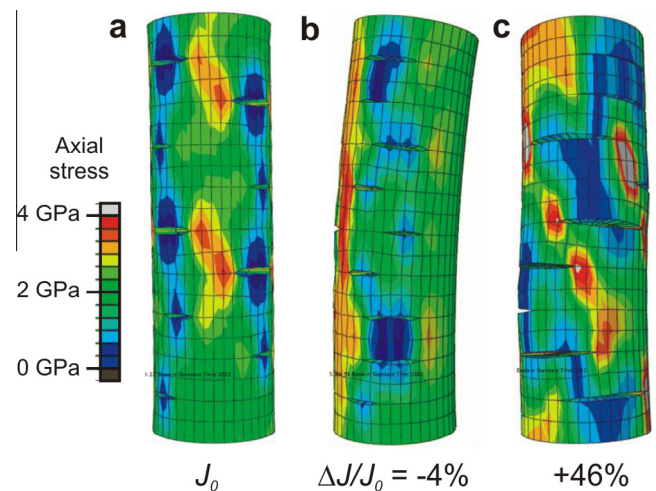


Fig. 6. Linear-elastic finite element analysis of local stresses and strain energy release rate (contour path integral  $J$ ) in CNF models containing different surface flaw configurations. (a) Small surface cracks equally distributed on the fiber.  $J_0$  represents the reference strain energy release rate. (b) Same surface cracks localized on one side of the fiber only.  $\Delta J/J_0$  represents the change in strain energy release rate. (c) Larger surface cracks. The total crack area is identical in all models.

toughness, is predicted to increase as  $N$  increases, due to the dissipative plastic processes as shown in Fig. 5b. This analysis therefore strongly supports the finding that the resistance to crack propagation in surface-bonded CNFs becomes optimal when the surface bond density increases.

#### 4. Conclusions

In summary, using detailed atomistic simulations of high-temperature annealing and tensile deformation in CNFs, we have found that the surface bond density linearly relates to the heat treatment temperature, and that the associated surface bond reconstruction can substantially increase both tensile strength and fracture energy by 65% and 622%, respectively, resulting in a regime of superplasticity unmatched by standard CNTs and graphitic nanofibers. This phenomenon results from the formation of ultra-strong surface bonds from bilayer edge folding that proved to be efficient in impeding interlayer sliding while promoting surface splaying processes. This computational study demonstrates that the surface bond density plays a key role in strengthening and crack growth resistance of CNFs, and suggests a simple means to structurally design better flaw-tolerant fibers for nanocomposites systems by optimizing the temperature of heat treatment.

#### Acknowledgments

The authors gratefully thank support from NASA EPSCoR Grants NNX07AT56A and NNX14AN20A, and the computer resources of the Vermont Advanced Computing Center under NASA Grant number NNX-08AO96G.

#### References

- [1] G.G. Tibbetts, M.L. Lake, K.L. Strong, B.P. Rice, *Compos. Sci. Technol.* 67 (2007) 1709–1718.
- [2] Y.-H. Qin, J. Yue, H.-H. Yang, X.-S. Zhang, X.-G. Zhou, L. Niu, W.-K. Yuan, *J. Power Sources* 196 (2011) 4609–4612.
- [3] C. Kim, K.S. Yang, *Appl. Phys. Lett.* 83 (2003) 1216–1218.
- [4] J. Sandler, P. Werner, M.S.P. Shaffer, V. Demchuk, V. Altstädt, A.H. Windle, *Composites Part A* 33 (2002) 1033–1039.
- [5] M.J. Palmeri, K.W. Putz, L.C. Brinson, *ACS Nano* 4 (2010) 4256–4264.
- [6] T. Uchida, D. Anderson, M. Minus, S. Kumar, *J. Mater. Sci.* 41 (2006) 5851–5856.
- [7] Y. Takahashi, H. Fujita, W.-H. Lin, Y.-Y. Li, T. Fujii, A. Sakoda, *Adsorption* 16 (2010) 57–68.
- [8] S. Lee, M.-S. Kim, A.A. Ogale, *Polym. Eng. Sci.* 50 (2010) 93–99.
- [9] T. Ozkan, Q. Chen, I. Chasiotis, *Compos. Sci. Technol.* 72 (2012) 965–975.
- [10] M. Endo, Y.A. Kim, T. Hayashi, K. Nishimura, T. Matusita, K. Miyashita, M.S. Dresselhaus, *Carbon* 39 (2001) 1287–1297.
- [11] Y.A. Kim, T. Matusita, T. Hayashi, M. Endo, M.S. Dresselhaus, *Carbon* 39 (2001) 1747–1752.
- [12] M. Endo, Y.A. Kim, T. Hayashi, T. Yanagisawa, H. Muramatsu, M. Ezaka, H. Terrones, M. Terrones, M.S. Dresselhaus, *Carbon* 41 (2003) 1941–1947.
- [13] J. Lawrence, L. Berhan, A. Nadarajah, *J. Nanoparticle Res.* 10 (2008) 1155–1167.
- [14] J.G. Lawrence, L.M. Berhan, A. Nadarajah, *ACS Nano* 2 (2008) 1230–1236.
- [15] T. Ozkan, M. Naraghi, I. Chasiotis, *Carbon* 48 (2010) 239–244.
- [16] J.J. Gu, F. Sansoz, *Carbon* 56 (2013) 351–357.
- [17] J.J. Gu, F. Sansoz, *Carbon* 66 (2014) 523–529.
- [18] S. Plimpton, *J. Comp. Phys.* 117 (1995) 1–19.
- [19] D.W. Brenner, O.A. Shenderova, J.A. Harrison, S.J. Stuart, B. Ni, S.B. Sinnott, *J. Phys. Condens. Matter* 14 (2002) 783.
- [20] Z.H. Xia, P.R. Guduru, W.A. Curtin, *Phys. Rev. Lett.* 98 (2007) 245501.
- [21] B. Peng, M. Locascio, P. Zapol, S. Li, S.L. Mielke, G.C. Schatz, H.D. Espinosa, *Nat. Nano* 3 (2008) 626–631.
- [22] M. Endo, Y.A. Kim, T. Hayashi, Y. Fukai, K. Oshida, M. Terrones, T. Yanagisawa, S. Higaki, M.S. Dresselhaus, *Appl. Phys. Lett.* 80 (2002) 1267–1269.
- [23] Z. Liu, K. Suenaga, P.J.F. Harris, S. Iijima, *Phys. Rev. Lett.* 102 (2009) 015501.
- [24] P. Koskinen, S. Malola, H. Häkkinen, *Phys. Rev. B* 80 (2009) 073401.
- [25] A. Stukowski, *Modelling Simul. Mater. Sci. Eng.* 18 (2010) 015012.
- [26] J.R. Rice, *J. Appl. Mech.* 35 (1968) 379–386.
- [27] Y.A. Zhu, Z.J. Sui, T.J. Zhao, Y.C. Dai, Z.M. Cheng, W.K. Yuan, *Carbon* 43 (2005) 1694–1699.
- [28] C. Wei, D. Srivastava, *Appl. Phys. Lett.* 85 (2004) 2208–2210.
- [29] V.R. Coluci, N.M. Pugno, S.O. Dantas, D.S. Galvão, A. Jorio, *Nanotechnology* 18 (2007) 335702.
- [30] K. Honjo, *Carbon* 41 (2003) 979–984.